Control Strategy for Starter Generator in UAV with Micro Jet Engine

Jun-ichi Itoh[1*], Kazuki Kawamura[1*], Hiroyuki Koshikizawa[2] and Kazuyuki Abe[2]
1 Department of Electrical, Electronics and Information Engineering, Nagaoka University of Technology, Niigata, Japan
2 Development Department, YSEC Co., Ltd, Niigata, Japan
*E-mail: itoh@vos.nagaokaut.ac.jp, k_kawamura@stn.nagaokaut.ac.jp

***Abstract*— This paper proposes control strategy of a starter generator connected to a jet engine for an unmanned aerial vehicle system. Thrust is generated by both the jet engine and propellers which are powered by the jet engine through the starter generator. A flight range can be extended since energy density of the jet engine in the developed system is higher than battery energy density in the conventional system. Moreover, the starter generator directly connects to the jet engine and rotates at high speed for miniaturization. The proposed control strategy achieves the starting, the powering and the cooling operations with the starter generator. It is confirm through an experiment of a 3-kW prototype, that the prototype system achieves the maximum conversion efficiency of 92.7%. The minimum generator current THD is 16.5% at 70000 r/min. Further, the exhaust nozzle temperature is controlled within the maximum deviation of 2% regarding to the command value in study state.**

Keywords*— *Starter generator, Jet engine, Unmanned aerial vehicle(UAV), V/f control.

I. Introduction

Recently, unmanned aerial vehicles (UAVs) have been actively studied for rescue activities in disaster [1–4]. In particular, the multicopter-type UAV has two advantages. First, it is easy to approach danger zones because of unmanned operation. Second, the multicopter-type UAV does not need a designated landing space. However, the multicopter-type is generally powered by batteries [2]. The flight range and carrying weight are limited because of the battery energy density [5]. Therefore, UAV with a jet engine has been developed [6]. In the developed UAV system, thrust is generated by both the jet engine and propellers which are powered by the jet engine through the starter generator. The flight range can be extended since the energy density of the jet engine is higher than the battery energy density. Furthermore, the developed UAV system is also be used as an emergency power supply owing to the starter generator.

An auxiliary power unit (APU) is generally used for starting and cooling the jet engine [7–8]. However, the use of APU leads to the increase in cost and size of the system. Furthermore, the rotation speed of the generator in APU is low because the generator is connected to the jet engine through reduction gears [9–10]. Therefore, the generator tend to be large in a high power capacity system.

In this paper, the UAV system with a jet engine and the control strategy of the starter generator are proposed. In the developed UAV system, only the starter generator is used for starting and cooling, which eliminates the use of APU. Furthermore, the starter generator connects directly to the jet engine and rotates at high speed for miniaturization. The challenge of this paper is the achievement of the stable operation through the proposed control strategy even when the starter generator transits among operation modes, i.e., starting mode, powering mode, and cooling mode without APU and reduction gears. In particular, the synchronous frequency command limiter and the output power limiter are used in the proposed control method. In addition, modulation method is modified by the estimated intersection phase based on synchronous PWM. Through the experiments, it is confirmed that the prototype achieves the maximum conversion efficiency of 92.7%, the minimum generator current THD of 16.5% at 70000 r/min. Further, the exhaust nozzle temperature is controlled within the maximum deviation of 2% compared to the command value in the steady state.

II. Developed UAV System

Figure 1 shows the configuration of the developed an UAV system. The jet engine and the starter generator are directly connected without reduction gears. The jet engine powers six propellers through the starter generator. In the aerial applications, weight reduction of the starter generator is required from the viewpoint of flight range. Thus, the starter generator is rotated at high speed for miniaturization and weight reduction.

Figure 2 shows the mode transition diagram of the developed UAV system. A host controller selects the operation mode. The operation modes are described as follows;

A. All Off Mode

This mode is a stationary state. The power converter is not operated(gate off).

B. Standby Mode

The DC/DC converter boosts the DC-link voltage from the battery voltage to 300 V.

C. Startup Mode

The starter generator is driven by the AC/DC converter in order to assist both the ignition of the jet engine and the acceleration up to 50000 r/min. The host controller controls the starter generator speed in this state. Further, the jet engine controls exhaust nozzle temperature.

D. Run Mode

The powering operation is performed in the range of the rotation speed from 50000 to 70000 r/min, and the battery is charged. The jet engine controls the speed, whereas the starter generator controls the output power.

E. Stop Mode

The engine output is halted, whereas the starter generator decelerates and cools the jet engine. When the exhaust nozzle temperature of the jet engine is cooled to 50°C or less, the operation of the power converter is stopped. Then, the operation mode is shifted to the all off mode.

III. Modulation Method for Even-order Harmonic Components Suppression

A. Continuous PWM

The starter generator is driven at the rotational speed of the jet engine, the carrier frequency, and the fundamental frequency are close to each other. This leads to the low-order harmonic components and the beat components on generator current. Thus, in the Run Mode, the nine-pulse synchronous PWM technique is used.

Figure 3 shows the voltage command with a modulation index of 0.8 and a triangular carrier with a frequency ratio of nine when the continuous PWM is applied. As shown Fig. 3(a), the voltage command v_u^* is compared with the triangular carrier to generate a PWM signal in general. As shown Fig. 3(b), the modulation index command V_m^* and the red carrier u_{mc} are compared to generate a PWM signal. The deformed carrier u_{mc} is calculated by

$$u_{mc} = \frac{u_m}{\sin\theta} \quad (\theta \neq 0°, 180°) \tag{1}$$

where θ is the phase of inverter voltage command and u_m is the triangular carrier.

The proposed modulation method estimates the intersection phase of the modulation signal and the carrier using a look-up table of the deformed carriers in the software, then outputs a voltage command according to the estimated intersection phase. It can be implemented in a micro-controller because this proposed modulation method is implemented without changing the hardware.

Table I shows the estimated intersection phase patterns of the continuous PWM. As shown in Table I, the estimated intersection phases of sectors zero and nine are determined to be 0° and 180° because of the synchronous PWM, respectively. The relationship between the phase and the modulation index command of the deformed carrier u_{mc} of the sectors 1, 2, 3, and 4 is tabulated as

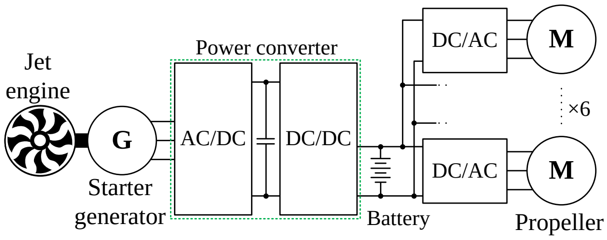

Fig. 1. Configuration of developed UAV system.

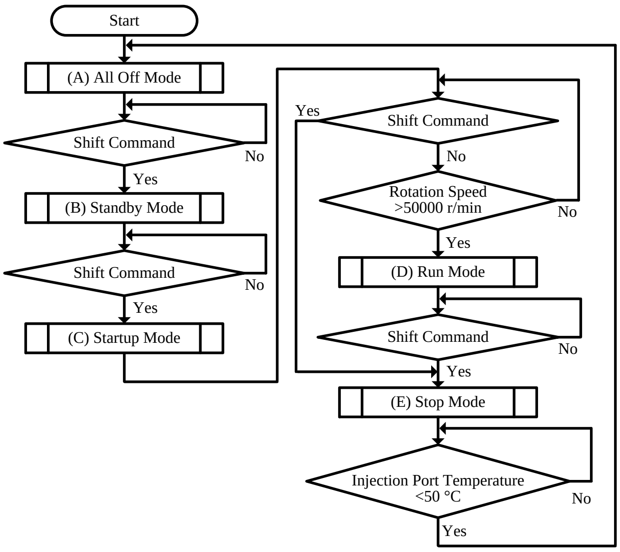

(a) Flowchart of developed UAV system operation.

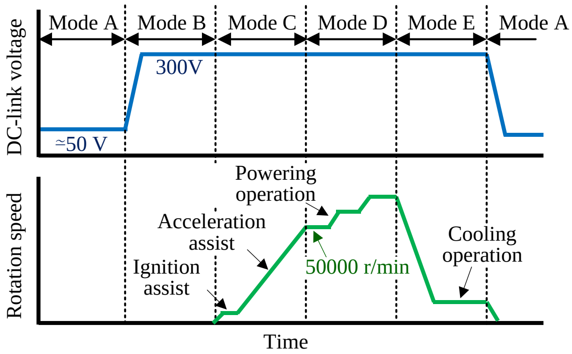

(b) Overview operation of jet generator.

Fig. 2. Mode transition diagram of developed UAV system.

look-up table 1, 2, 3, and 4. Note that α_1, α_2, α_3 and α_4 are the estimated intersection phases referred from these look-up tables. For the sector 5 and later, it is not necessary to prepare the tables in order to estimate the phase using the symmetry each 90°. The proposed modulation method acquires the estimated intersection phase in each sector using the phase referred to from look-up table 1 to 4 and the relationship in Table I, and outputs a voltage command according to the estimated intersection phase. The generated PWM signal is equivalent to that generated by analog control. Therefore, even-order harmonic components do not occur in PWM signal.

B. Discontinuous PWM

Figure 4 shows a modulation signal and a carrier with frequency ratio of 9 and a modulation index of 0.8 when

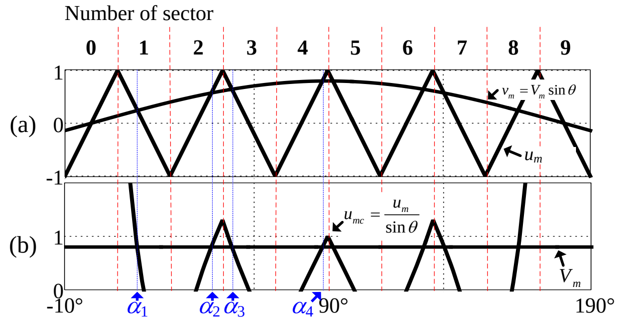

Fig. 3. Waveforms of voltage commands and carriers with continuous PWM.

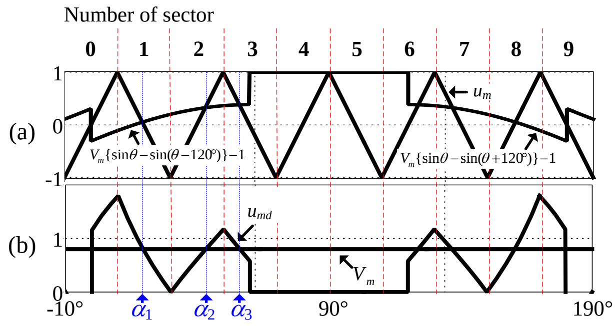

Fig. 4. Waveforms of voltage commands and carriers with discontinuous PWM.

TABLE I
Proposed estimated phase patterns of continuous PWM.

Sector	Look Up Table	Phase of Intersection Point	Sector	Look Up Table	Phase of Intersection Point
0		0°	9		180°
1	1	α_1	10	1	180°+α_1
2	2	α_2	11	2	180°+α_2
3	3	α_3	12	3	180°+α_3
4	4	α_4	13	4	180°+α_4
5	4	180°-α_4	14	4	360°-α_4
6	3	180°-α_3	15	3	360°-α_3
7	2	180°-α_2	16	2	360°-α_2
8	1	180°-α_1	17	1	360°-α_1

α_X : Phase by Look Up Table X

TABLE II
Proposed estimated phase patterns of discontinuous PWM.

Sector	Look Up Table	Phase of Intersection Point	Sector	Look Up Table	Phase of Intersection Point
0		0°	9		180°
1	1	α_1	10	1	180°+α_1
2	2	α_2	11	2	180°+α_2
3	3	α_3	12	3	180°+α_3
4		90°	13		270°
5		90°	14		270°
6	3	180°-α_3	15	3	360°-α_3
7	2	180°-α_2	16	2	360°-α_2
8	1	180°-α_1	17	1	360°-α_1

α_X : Phase by Look Up Table X

the discontinuous PWM is employed. The discontinuous PWM signal v_{xd}^* shown in Fig. 4(a) is calculated by adding the following offset to the three phase modulation signal v_x.

$$v_{xd}^* = v_x^* + v_{offset}^*, \quad (x = u, v, w)$$

$$v_{offset}^* = \begin{cases} 1 - |v_{\max}| & \text{if } |v_{\max}| \geq |v_{\min}|, \\ -1 + |v_{\min}| & \text{if } |v_{\min}| < |v_{\max}|, \end{cases} \quad (2).$$

$$\text{and} \begin{cases} v_{\max} = \max[v_u^*, v_v^*, v_w^*] \\ v_{\min} = \min[v_u^*, v_v^*, v_w^*] \end{cases}$$

As mentioned in Section A, a deformed carrier u_{md} in Fig. 4(b) is used. The intersection phases in sectors 0 and 4 are defined as 0° and 90° in advance, respectively. Therefore, the deformed carriers of sectors 1, 2 and 3 are only required to estimate the intersection phases. The deformed carrier u_{md} is calculated by

$$u_{md} = \frac{u_m + 1}{\sin\theta - \sin(\theta - 120°)} \quad (10° \leq \theta < 60°) \quad (3).$$

Note that in the section of more than 60° in sector 3, the intersection phase is set to 60° when the modulation index is 0.577 or less.

Table II shows the estimated intersection phase patterns of the discontinuous PWM. The relationship between the phase and the modulation index command of the deformed carrier u_{md} of the sector 1, 2, and 3 is defined as in look-up table 1, 2, and 3. By referring the phases α_1, α_2, α_3 using the modulation index from these look-up tables, the intersection phase of the carrier and the modulation signal in each sector is estimated by the relationship shown in Table II. By using this method, the symmetry of the PWM signal is secured even in the discontinuous modulation, and the even-order harmonic components do not occur in the PWM signal.

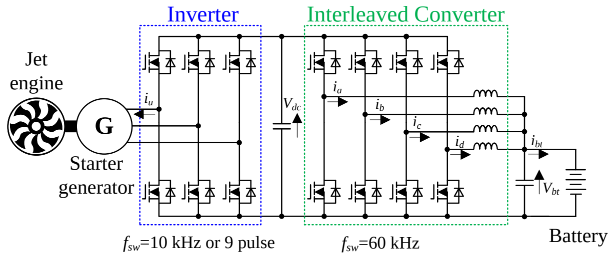

Fig. 5. Configuration of power converter.

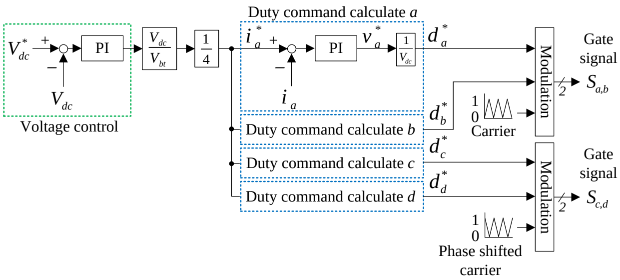

Fig. 6. Control block diagram of DC/DC interleaved converter.

IV. Control Strategy for Starter Generator

Figure 5 shows the configuration of the power converter. This converter consists of a three-phase inverter and a four-leg interleave DC/DC converter. Since the battery voltage is approximately 50 V, the DC/DC converter is required to boost the voltage to 300 V in order to drive the inverter.

Figure 6 shows the control block diagram of DC/DC interleaved converter. The DC link voltage V_{dc} is regulated to the command value. The current imbalance among four legs is suppressed by the current control of

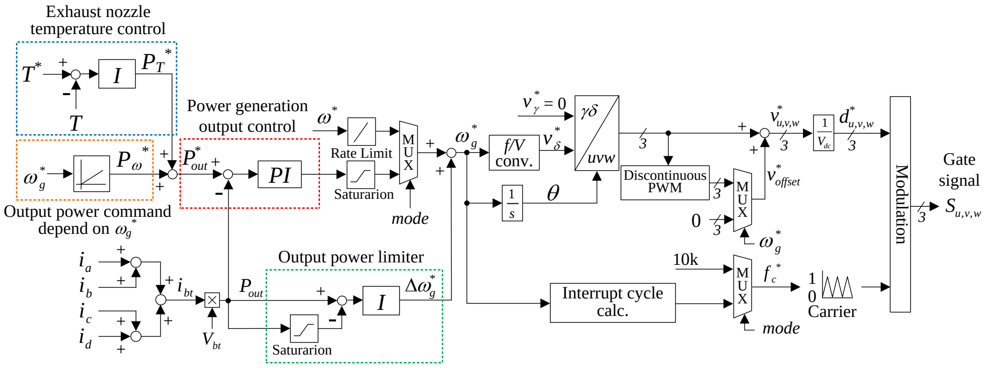

Fig. 7. Control block diagram of 3-phase inverter.

each leg. Moreover, the carrier of each two legs is phase shifted by half a period compared to the other two legs. As a result, the switching frequency is equivalently doubled and the current ripple is reduced to half [11].

Figure 7 shows the control block diagram of the three phase inverter. The power control is operated in the run mode, whereas the V/f control is employed in the other modes. The rotation speed of the jet engine is suddenly reduced because the output power of the jet engine is not sufficiently high when the inverter control switched from the V/f control to the output power control or exhaust nozzle temperature control for the run mode. In other words, the self-sustained operation of the jet engine is difficult at the low speed. In order to solve this problem, a synchronous frequency command limiter is applied. As a result, the speed is kept constant until the jet engine output becomes sufficiently high. During the startup mode, the generator torque suddenly changes. In order to prevent overcurrent in this operation, an output power limiter is introduced. Consequently, the synchronous frequency command is compensated in order to avoid the sudden change in the torque. Furthermore, around the rated speed, discontinuous PWM is employed to deal with overmodulation region.

V. Stabilization Analysis of Power Generation Output Control

Figure 8 shows the characteristics of jet engine thrust against the rotation speed. As shown Fig. 8, a thrust of 68.0 N is obtained at the rotation speed of 70000 r/min. Under the atmospheric pressure, the atmospheric temperature, and the air density are constant, the thrust of the jet engine depends only on the rotational speed regardless of the output power. Since the thrust of the jet engine is proportional to the cube of the rotational speed, the thrust F obtained by the measured value is approximated by the cube of the rotational speed as follows;

$$F = k_F \omega^3 \tag{4}$$

where ω is rotation speed of the jet engine and k_F is coefficient obtained from the measured value.

Figure 9 shows the block diagram of the output power control system with a jet engine. In this system, the generator synchronous angular frequency ω_g is produced

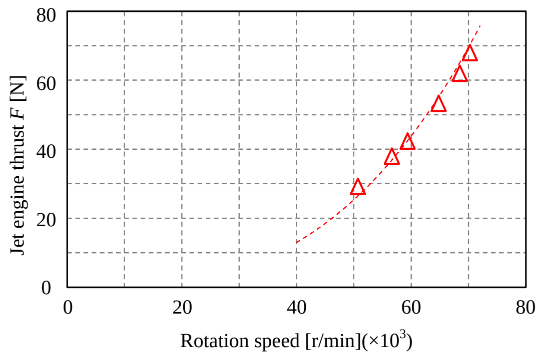

Fig. 8. Characteristics of jet engine thrust.

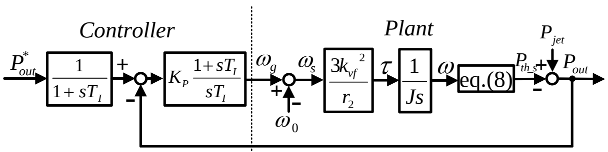

Fig. 9. Block diagram of output power control system with jet engine.

by the difference between the output power command P_{out}^* and the output power detection value P_{out}. Further, it is assumed that the response of the rotation speed control for the jet engine is sufficiently slower than that of the output power control. By ignoring the loss, the total power of the jet engine P_{jet} is calculated by

$$P_{jet} = P_{th} + P_{out} \tag{5}$$

where P_{th} is the thrust power of the jet engine. This thrust power is added to the shaft power P_{out} that drives the propeller. This shaft power is determined by the flight speed and the thrust of the aircraft. However, if the aircraft is stationary as in the test, the shaft power cannot be calculated from the flight speed. In this case, the stationary shaft power P_{th_s} is calculated by

$$P_{th\_s} = \frac{F}{11.2} \times 736 \tag{6}$$

Substituting (4) into (6) and setting the coefficient as k_{th}, the stationary shaft power [12] is calculated by

$$P_{th\_s} = \frac{736 k_F}{11.2} \omega^3 = k_{th} \omega^3 \tag{7}$$

In order to analyze the stability of the control, the rotation angular velocity is linearized around the steady-state points.

$$P_{th\_s} = 3 k_{th} \omega_0^{\ 2} \omega \tag{8}$$

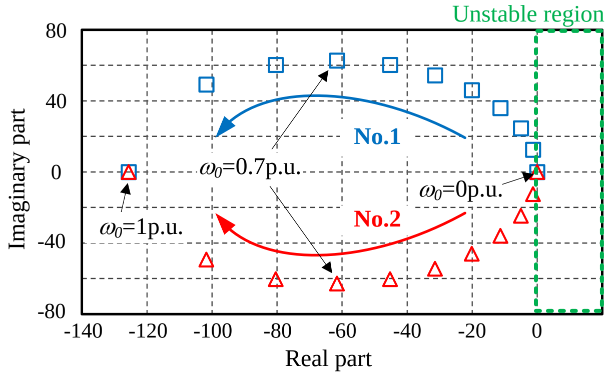

Fig. 10. Roots locus when the initial angular velocity ω_0 is increased.

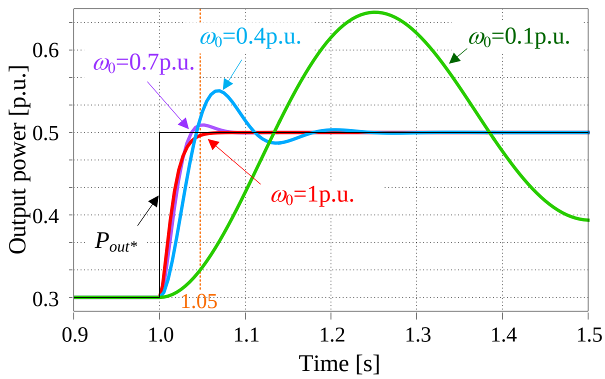

Fig. 11. Step response of output power when output power command is changed from 0.3 p.u. to 0.5 p.u.

Note that ω_0 is the initial angular velocity at the steady-state point. Consequently, the transfer function from input to output of this control system is expressed by

$$G(s) = \frac{-\dfrac{9K_p k_{vf}{}^2 k_{th}\omega_0{}^2}{K_i r_2 J}}{s^2 - \dfrac{9K_p k_{vf}{}^2 k_{th}\omega_0{}^2 s}{r_2 J} - \dfrac{9K_p k_{vf}{}^2 k_{th}\omega_0{}^2}{K_i r_2 J}} \quad (9),$$

where K_p is the proportional control gain, K_i is the integral control gain, k_{vf} is the voltage coefficient in the v/f control, J is the total inertia of the jet engine and generator, and r_2 is the secondary winding resistance of the generator. Furthermore, K_p and K_i are expressed as functions of the damping coefficient ζ and the response angular frequency ω_n.

$$K_p = -\frac{2\xi\omega_n r_2 J}{9k_{vf}{}^2 k_{th}\omega_0{}'^2} \quad (10)$$

$$K_i = \frac{2\xi}{\omega_n} \quad (11)$$

Note that ω_0' is the initial angular velocity. This angular velocity should be set accordingly to the detection value of the angular velocity. However, the angular velocity detection is not employed in the test; therefore, this value is predetermined as following.

Figure 10 shows the roots locus when the initial angular velocity ω_0 is increased. In this system, the powering operation is performed in the rotation speed range from 0.7 to 1.0 p.u. Therefore, the initial angular velocity setting value ω_0' is 0.7 p.u. The damping coefficient ζ is set to 0.7. The response angular frequency ω_n is set; thus, the overshoot time is 0.05 seconds, which is 1/10 of the jet engine control period of 0.5 seconds. As shown in Fig. 10, when the rotation speed is 0 p.u., the control system is at the stability limit because the poles locate on the imaginary axis. The control system becomes stable because the poles move to the negative half plane when the rotation speed is larger than 0 p.u.

Figure 11 shows the step response of output power when output power command is changed from 0.3 p.u. to 0.5 p.u. As shown in Fig. 11, at a rotation speed of 0.7 p.u. and 1.0 p.u., the response is equal to or larger than the design response time. The response time is delayed and a large overshoot occurs in output power at the rotation speed of 0.4 p.u. and 0.1 p.u., which is the low-speed range. However, such large overshoot does not occur since the power generation operation is performed only in the high-speed range in this system.

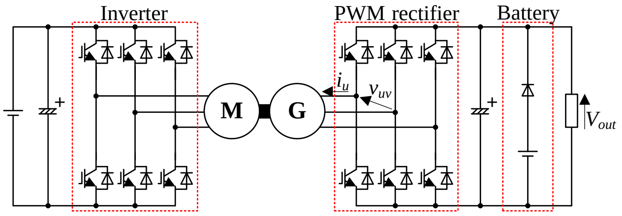

Fig. 12. Configuration of experimental system.

TABLE III
Specification of starter generator.

Parameter	Value
Poles	2
Rated rotary field speed	70000 r/min
Rated speed	68271 r/min
Rated voltage	200 V
Rated current	15.3 A
Rated power	4 kW
Rated torque	0.6 N・m
Weight	3.0 kg
Diagram	110 mm
Full length	192 mm

VI. Experimental Results

A. Modulation method for even-order harmonic components suppression

Figure 12 shows the experimental system. Table III shows the specification of the starter generator. In this test, two motors shown in Table III are connected instead of the jet engine. In addition, a small capacity DC regulated power supply is connected to supply the excitation current at the time of starting since the starter generator is an induction generator.

Figure 13 shows a block diagram of the PWM converter. This control system is adjust the slip angle frequency and control the DC-link voltage. In the high speed range, switching from the asynchronous PWM to the synchronous PWM. Furthermore, around the rated speed, discontinuous PWM is employed to deal with the overmodulation region.

Figure 14 shows the operation waveforms of the continuous PWM at frequency ratio of nine and the rotation speed of 0.8 p.u. The modulation index is 0.871, and both the conventional method and the proposed method control the output voltage to be constant at 300 V.

Figure 15 shows the harmonic analysis results of the generator current of the continuous PWM. As shown Fig. 15(b), the proposed method suppresses low even-order harmonic components, such as second, eighth, and tenth order, which are generated by the conventional method.

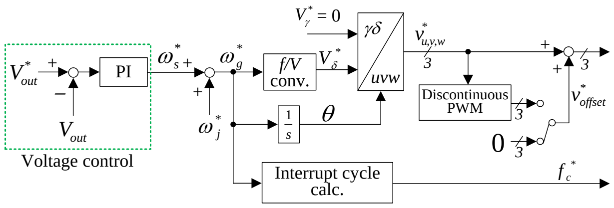

Fig. 13. Block diagram of PWM converter.

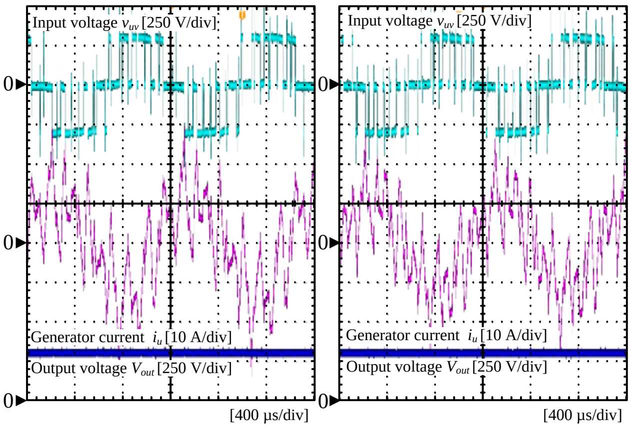

(a) Conventional method. (b) Proposed method.

Fig. 14. Experimental results of continuous PWM.

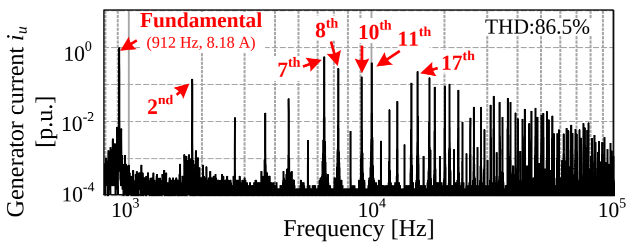

(a) Conventional method.

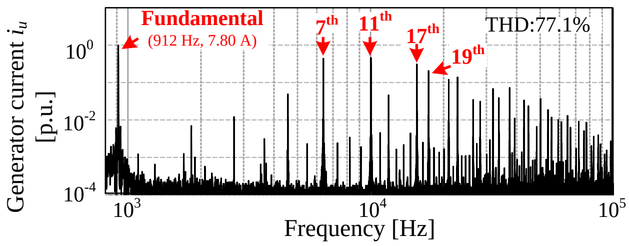

(b) Proposed method.

Fig. 15. Frequency analysis results of continuous PWM.

Also, the eighth harmonic component was reduced by 99.2% compared to the conventional method. In addition, the generator current total harmonic distortion (THD) is reduced by 9.99% compared to the conventional method.

Figure 16 shows the operation waveforms of the discontinuous PWM at a frequency ratio of nine and a rotation speed of 1.0 p.u. The modulation index is 1.08, and both the conventional method and the proposed method control the output voltage to be constant at 300 V.

Figure 17 shows the harmonic analysis results of the generator current of the discontinuous PWM. As Fig. 17(b) shown, the proposed method suppresses low even-order harmonic components, such as second, eighth, and tenth order, which are generated by the conventional method. Also, the eighth harmonic component was reduced by 99.1% compared to the conventional method. In addition, the generator current THD is reduced by 7.14% compared to the conventional method. Therefore, this method is effective also in the discontinuous PWM.

B. Control strategy for starter generator

Figure 18 and Table IV shows the prototype of the jet generator and the specifications of the jet engine. As

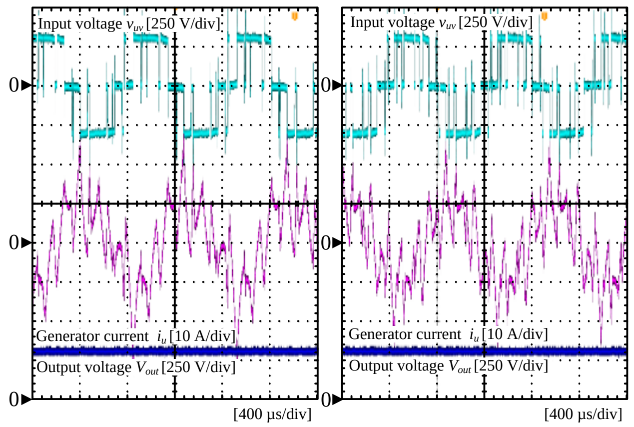

(a) Conventional method. (b) Proposed method.

Fig. 16. Experimental results of discontinuous PWM.

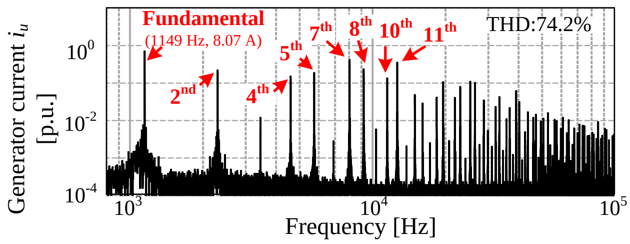

(a) Conventional method.

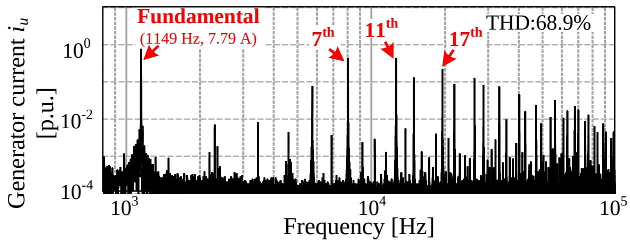

(b) Proposed method.

Fig. 17. Frequency analysis results of discontinuous PWM.

shown in Fig. 18, the starter generator is connected to the jet engine without a speed reduction gear.

Figure 19 shows the experimental waveforms of Run Mode at the rotation speeds of 70000 r/min, where the output power to the battery is 2.98 kW. As shown in Fig. 19, the DC link voltage is regulated to 300 V. Furthermore, the stable power generation operation is achieved since the battery current is constant at any rotation speeds.

Figure 20 shows the harmonic analysis results of the generator current in Fig. 19. As shown in Fig. 20, even-order low harmonic components are less than 0.2% which is sufficiently smaller than the fundamental component.

Figure 21 shows the characteristics of the generator current THD against output power. As shown in Fig. 21, the minimum current THD of 16.5% is achieved at the rotation speed of 70000 r/min and the output power of 2.98 kW. This is because the fundamental component of the generator current increases as the output power increases.

Figure 22 shows the efficiency characteristics of the power converter. As shown in Fig. 22, the maximum efficiency of 92.7% is achieved at the rotation speed of 70000 r/min and the output power of 2.98 kW.

Figure 23 shows the temperature characteristics of the exhaust nozzle against rotation speed and the output power when the ambient temperature is 26°C. As shown in Fig. 23, as the rotation speed of the jet engine increases, higher the output power is obtained at the same exhaust nozzle temperature. Further, this system has the highest efficiency when the exhaust nozzle temperature is around 800°C. Therefore, an output power command depends on angle frequency command ω_g^* is as shown in Fig. 23.

Figure 24 shows the experimental results the jet generator operation with the exhaust nozzle temperature control. The exhaust nozzle temperature command is 800°C. The jet engine is accelerated to 60000 r/min, 65000 r/min, and 70000 r/min in the run mode. Then the jet engine is decelerated to 60000 r/min. As shown in Fig 24, even when the rotation speed accelerates or decelerates, the exhaust nozzle temperature converges to the command value. The exhaust nozzle temperature can be controlled within the maximum deviation of 2% compared to the command value in the steady state. Furthermore, the exhaust nozzle temperature at 70000 r/min drops to 700°C because the inflow current of the battery is limited. In addition, the proposed control method achieves among the starting, the powering and the cooling operations. The transition without the deceleration is achieved by the synchronous frequency command limiter when the startup mode changes to the run mode. The output power gradually approaches zero after this transition, because the starter generator maintains the rotation speed until the output power of the jet engine becomes sufficiently high. The acceleration without overload is achieved in the startup mode by an output power limiter, which limits a command up to 1 kW. Further, the starter generator decelerates by a free run when the operation mode transitions to the stop mode from the run mode. Then the inverter restarts at a rotation speed of 1000 r/min. The starter generator simultaneously performs the cooling operation.

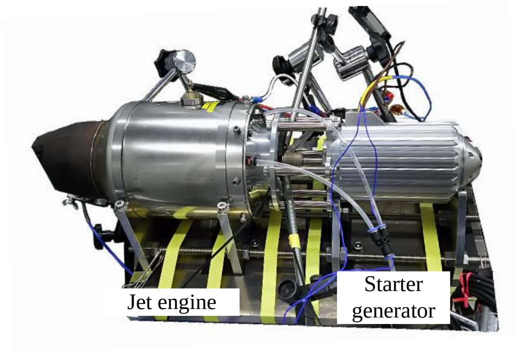

Fig. 18. Prototype of jet generator.

TABLE IV
Specification of jet engine.

Parameter	Value
Weight	2.9 kg
Diameter	131 mm
Full length	281 mm
Rated thrust	165 N
Rated speed	100000 r/min

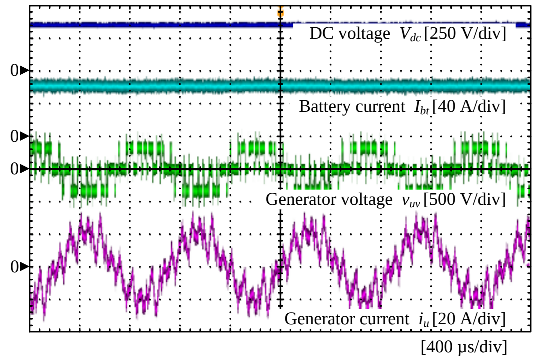

Fig. 19. Experimental waveforms of Run Mode.

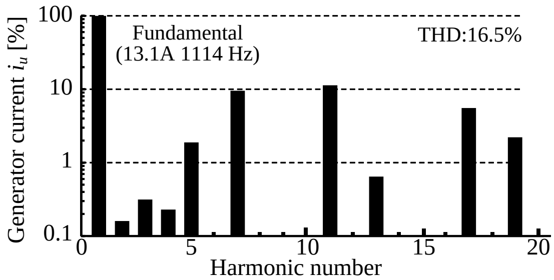

Fig. 20. Harmonic components on the generator current.

VII. Conclusion

The control strategy for UAV with the jet engine were proposed in this paper. The stable transition without decelerating and overcurrent between the operation modes of the starter generator was achieved by the synchronous frequency command limit and the output power limiter. In addition, the even-order low harmonic

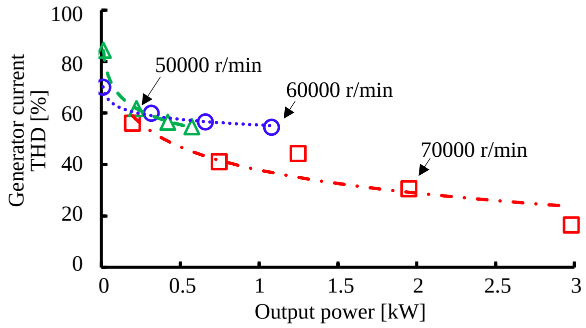

Fig. 21. Characteristics of generator current total harmonics distortion.

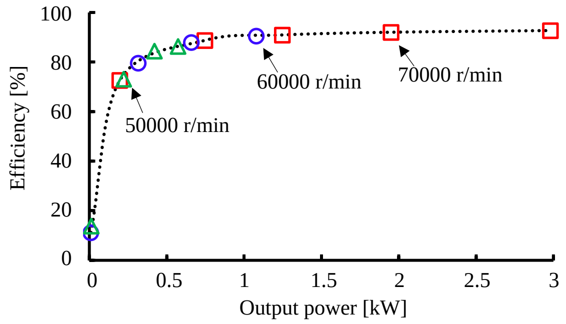

Fig. 22. Characteristics of efficiency of power converter.

components are suppressed by the modulation method using the estimated intersection phase for the synchronous PWM. The 3-kW prototype system achieved the maximum conversion efficiency of 92.7%, the minimum generator current THD of 16.5% at 70000 r/min. Further, the exhaust nozzle temperature was controlled within the maximum deviation of 2% of the command value.

ACKNOWLEDGMENT

This paper is based on results obtained from a project subsidized by the New Energy and Industrial Technology Development Organization (NEDO) of Japan.

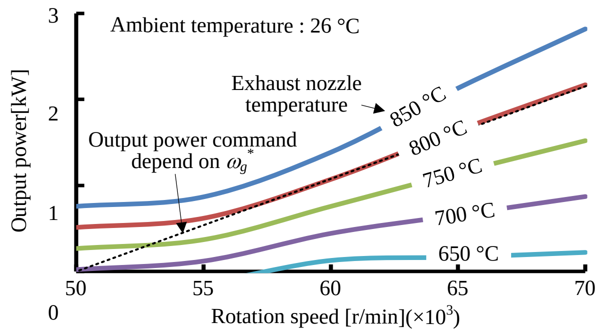

Fig. 23. Characteristics of exhaust nozzle temperature against rotation speed and output power, and output power command according to rotation speed.

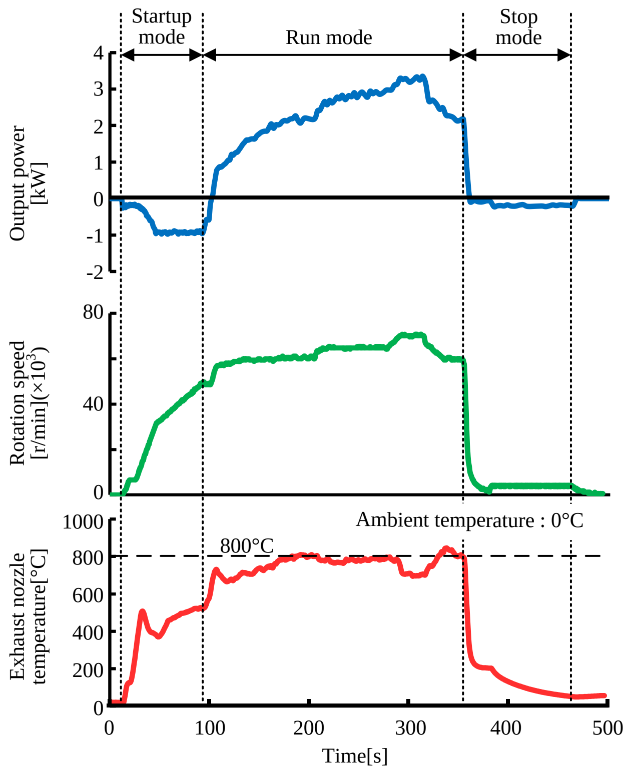

Fig. 24. Experimental results of operation of jet generator.

REFERRENCES

[1] A. C. Satici, H. Poonawala, M. W. Sppong:"Robust Optical Control of Quadrotor UAVs", IEEE Access, vol. 1, pp. 79-93, 2013.

[2] N. Gageik, P. Benz, S. Montenegro:"Obstacle Detection and Collision Avoidance for a UAV With Complementary Low-Cost Sensors", IEEE Access, vol. 3, pp. 599-609, 2015

[3] J. Shiau, D. Ma, P. Yang, G. Wang, J. Gong:"Design of a Solar Power Management System for an Experimental UAV", IEEE Transactions on Aerospace and Electronic Systems, vol. 45, No. 4, pp. 1350-1360, 2009

[4] J. Shiau, D. Ma, P. Yang, G. Wang, J. Gong:"Predictor-Based Control of a Class of Time-Delay Systems and Its Application to Quadrotors", IEEE Transactions on Industrial Electronics, vol. 64, No. 4, pp. 459-469, 2016

[5] M. Whittingham "History, Evolution, and Future Status of Energy Storage", Proceedings of the IEEE, vol. 100, pp. 1518-1534, 2012

[6] "Small UAV turbojet engine developed in Japan". http://robohub.org/small-uav-tarbojet-engine-developed-in-japan/

[7] S. Chuangpishit, A. Tabesh, Z. Shahrbabak M. Saeedifard:"Topology Design for Collector Systems of Offshore Wind Farms With Pure DC Power Systems", IEEE Transactions on Industrial Electronics, vol. 61, No. 1, pp. 320-328, 2014

[8] Yosei Hirano, Takashi Yoshida, Kiyoshi Ohishi, Toshimasa Miyazaki, Yuki Yokokura, and Masataka Sato,"Vibration Suppression Control Method for Trochoidal Reduction Gears under Load Conditions", IEEJ J. Industry Applications, vol.5, no.3, pp.267-275, 2016

[9] Takashi Yoshioka, Thao Tran Phuong, Akinori Yabuki, Kiyoshi Ohishi, Toshimasa Miyazaki, and Yuki Yokokura," High-performance Load Torque Compensation of Industrial Robot using Kalman-filter-based Instantaneous State Observer", IEEJ J. Industry Applications, vol.5, no.3, pp.267-275, 2016.

[10] H. Kim, S. B. Lee, S. Park, S. H. Kia and G. A. Capolino, "Reliable Detection of Rotor Faults Under the Influence of Low-Frequency Load Torque Oscillations for Applications With Speed Reduction Couplings," IEEE Transactions on Industry Applications, vol. 52, no. 2, pp. 1460-1468, 2016

[11] Toshiki Nakanishi, and Jun-ichi Itoh,"Control Strategy for Modular Multilevel Converter based on Single-phase Power Factor Correction Converter", IEEJ J. Industry Applications, vol.6, no.1, pp.46-57, 2017.

[12] E. Torenbeek: "Synthesis of Subsonic Airplane Design", Kluwer Academic Publishers, pp. 97-140, 2014